Bursty Bulk Flow Turbulence as a Source of Energetic Particles to the Outer Radiation Belt

R. E. Ergun[1,2], M. E. Usanova[2], D. L. Turner[3], and J. E. Stawarz[4]

Corresponding author: Robert E. Ergun, Laboratory of Atmospheric and Space Sciences, University of Colorado, Boulder, Colorado, USA 80303. ree@lasp.colorado.edu.

[1] Department of Astrophysical and Planetary Sciences, University of Colorado, Boulder, Colorado, USA.

[2] Laboratory for Atmospheric and Space Physics, University of Colorado, Boulder, Colorado, USA.

[3] Johns Hopkins University Applied Physics Laboratory, Laurel, MD, USA

[4] The Blackett Laboratory, Imperial College London, United Kingdom

Key Points:

A bursty bulk flow near the outer radiation belt displays turbulent electric fields and enhanced fluxes of energetic ions and electrons.

Electrons appear to be locally accelerated by turbulent electric fields forming an energetic shoulder in the distribution.

Turbulent electric fields in the BBF braking region favors energization of the highest energy electrons.

Abstract

We report observations of a Bursty Bulk Flow (BBF) penetrating close to the outer edge of the radiation belt. The turbulent BBF braking region is characterized by ion velocity fluctuations, magnetic field (***B***) variations, and intense electric fields (***E***). In this event, energetic (>100 keV) electron and ion fluxes are appreciably enhanced. Importantly, fluctuations in energetic electrons and ions suggest local energization. Using correlation distances and other observed characteristics of turbulent ***E***, test-particle simulations support local energization by ***E*** that favors higher-energy electrons and leads to an enhanced energetic shoulder and tail in the electron distributions. The energetic shoulder and tail could be amplified to MeV energies by adiabatic transport into the radiation belt where |***B***| is higher. This analysis suggests that turbulence generated by BBFs can, in part, supply energetic particles to the outer radiation belt and that turbulence can be a significant contributor to particle acceleration.

1. Introduction

Turbulence, by its very nature, cascades energy in driven systems to smaller scales at which dissipation takes place. In Earth's magnetotail, the energy source is often magnetic field (***B***) annihilation enabled by magnetic reconnection, the associated ion jet ($\boldsymbol{V}_{Ion}$), or Poynting flux. As ***B*** and $\boldsymbol{V}_{Ion}$ energy cascades to smaller scales, the electric field (***E***) follows suit to carry out the transfer of ***B*** and $\boldsymbol{V}_{Ion}$ energy into thermal energy. We hypothesize that, for electrons in a magnetized plasma, those with the highest energies have the largest gyroradii and largest parallel velocities, so they receive energy from both large- and small-scale ***E*** fluctuations. Particles with the lowest energies are last in line as they receive energy only from the smallest scales of ***E***. As a result, turbulent energization favors energetic particles, which results in acceleration.

In this letter, we concentrate on electron energization on closed field lines in the turbulent environment created by Bursty Bulk Flows (BBFs, Baumjohann et al., 1989; Angelopoulos et al., 1992; 1994). BBFs account for a significant fraction of energy transport from the Earth's magnetotail to the outer radiation belt and can lead to aurora (e.g., Sergeev et al., 1999; 2000; Nakamura et al., 2001; Sergeev et al., 2014; Ergun et al., 2015; Stawarz et al., 2015; Turner et al., 2015; 2016; 2021). They usually originate in the magnetotail beyond ~15 R_E (Earth radius) by magnetic reconnection events that are localized in the GSM *Y* (Geocentric Solar Magnetospheric) direction (Ohtani, Singer, and Mukai, 2006; Runov et al., 2009; 2011; Sitnov, Swisdak, and Divin, 2009). BBFs often are accompanied by "dipolarization" in which stretched ***B*** in the magnetotail, dominated by its GSM *X* component, relaxes to a more dipole-like configuration. Dipolarization supports the hypothesis that BBFs are earthward-flowing magnetic reconnection exhaust (e.g., Sitnov, Swisdak, and Divin, 2009; Nakamura, et al. 2009).

The characteristics of BBFs at distances greater than ~8 R_E from Earth are fairly well described (e. g. Zhang et al., 2016). At >12 R_E, earthward flow velocities can reach up to 1000 km s^{-1} (Angelopoulos et al., 1992; 1994). Flow velocities slow to the order of 100 km s^{-1} as BBFs travel from ~12 R_E to ~8 R_E due to stronger $\boldsymbol{B}$ and higher densities. This region, called the BBF braking region, frequently displays strong turbulence along with energized ions and electrons (Stawarz et al, 2015; Ergun et al., 2015).

Properties of BBFs are less well understood inside of ~8 R_E. One of the key unknowns is how BBFs are related to enhancements of energetic particles in the outer radiation belts known as flow injections. Inside of ~8 R_E, the flow speeds of the progenitor BBFs are dramatically reduced and dipolarization is difficult to identify in the strong $\boldsymbol{B}$ environment, so correlation between BBFs and flow injections is challenging (Takada et al, 2006; Ohtani, Singer, and Mukai, 2006; Dubyagin et al, 2011, Sergeev et al., 2012; Liu et al., 2016).

Observations show that a subset of particularly strong BBFs generate turbulence in the braking region with intense $\boldsymbol{E}$ (Ergun et al., 2015; Stawarz et al, 2015). Fluctuations in electron temperature (T_e), ion temperature (T_i), and in energetic fluxes indicate possible local energization (Usanova and Ergun, 2022). Here, we investigate processes by which electrons are energized in the turbulent BBF braking region. The Magnetospheric Multiscale (MMS) mission (Burch et al., 2016) has four satellites that, at the time, are separated by distances ranging from ~39 to ~123 km, which allows us to determine properties of the turbulent $\boldsymbol{E}$ including a constraint on the correlation distances.

In this letter, the term "energization" implies generic energy input to a species, "heating" is a thermal process in the core of a distribution, and "acceleration" is the development of a non-thermal tail. Particle energization is expected in the turbulent BBF braking region. However, a critical aspect is how the energy is distributed within the electron and ion distributions. Core heating results in an increase in temperature. If energization favors energetic particles, non-thermal distributions develop. Here, we show that the observed properties of ***E*** could result in non-thermal electron distributions that may seed the outer radiation belt.

2. Observations

Figure 1 displays a BBF with turbulent ***E***. The data are from the MMS satellites, which are, in this event, located in the southern magnetosphere. Figure 1a displays ***B*** in GSM coordinates over a 50-minute period. Colors represent direction and the black trace is |***B***|. A magnified view of B_x is in panel b with a dashed line to highlight dipolarization. B_z shows little net change, likely due to the off-equatorial position of MMS. Immediately below, panel c plots ***B*** 10-s detrended, $\boldsymbol{dB} = \boldsymbol{B} - \langle\boldsymbol{B}\rangle_{10s}$, which accentuates fluctuations in ***B***. Panels d, e, f, and g plot, respectively, ion flux as a function of energy from 70 to 600 keV, differential ion energy flux from 3 eV to 25 keV, electron flux from 60 to 500 keV, and differential electron energy flux from 6 eV to 25 keV. The MMS instruments are described in a series of articles (Torbert et al., 2016, Russell et al., 2016; Le Contel et al., 2016; Lindqvist et al., 2016, Ergun et al., 2016; Mauk et al., 2016; Pollock et al., 2016).

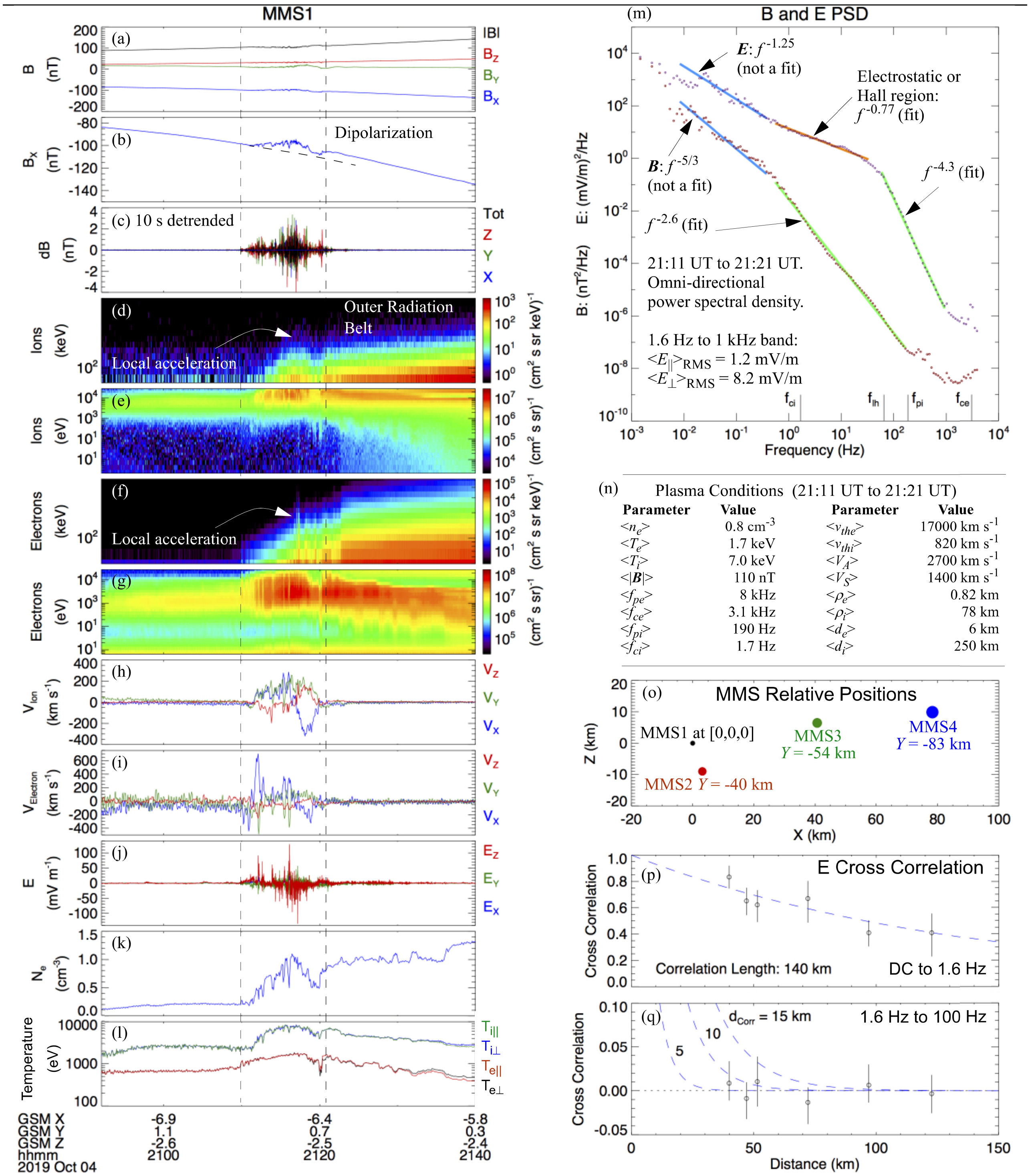

Figure 1. MMS1 observations of a BBF penetrating close to the outer radiation belt. The horizontal axis on the left column is 50 minutes in time. Vectors are in GSM coordinates; colors represent components as marked on the right of a panel. (a) ***B*** at 62.5 ms resolution. The black

trace is |$\boldsymbol{B}$|. (b) A magnified view of B_x. (c) $\boldsymbol{B}$ detrended by 10 s. (d) Ion flux as a function of energy (vertical axis) from 70 to 600 keV. These data are from all four MMS spacecraft. (e) Differential ion energy flux as a function of energy from 3 eV to 25 keV. (f) Electron flux from 60 to 500 keV. (g) Differential electron energy flux 6 eV to 25 keV. (h) $\boldsymbol{V}_{Ion}$ at 4.5 s resolution. (i) $\boldsymbol{V}_{Elc}$ at 4.5 s resolution smoothed over 13.5 s. (j) $\boldsymbol{E}$ at 31.25 ms resolution. (k) Electron density at 4.5 s resolution. (l) T_i and T_e at 4.5 s resolution. (m) The PSD of $\boldsymbol{B}$ and $\boldsymbol{E}$ versus frequency. (n) Average plasma conditions. (o) The relative positions of the MMS spacecraft. (p) The cross-correlation of $\boldsymbol{E}$ between the MMS spacecraft plotted as a function of separation. $\boldsymbol{E}$ is filtered from DC to 1.6 Hz. (q) The cross-correlation of $\boldsymbol{E}$ filtered from 1.6 Hz to 100 Hz.

At the beginning of Figure 1, ~20:50 UT, the MMS satellites are in a relatively quiet region of the magnetotail (auroral electrojet index ~100 nT). A noticeable event begins at ~21:10 UT and endures until ~21:21 UT. During this period, $\boldsymbol{B}$ dipolarizes (Figure 1b) and has visible fluctuations (Figure 1c). There is an enhancement of energetic (>100 keV) ion and electron fluxes (panels d-g). Importantly, the energetic fluxes are varying, implying possible local acceleration. At the same time, $\boldsymbol{V}_{Ion}$ (Figure 1h) indicates disturbed flow over 200 km/s including a flow vortex (Birn et al., 1997; Gabrielse et al., 2012; Sergeev et al., 2014). The electron velocity fluctuations ($\boldsymbol{V}_{Elc}$, Figure 1i) differ from $\boldsymbol{V}_{Ion}$ indicating Hall $\boldsymbol{E}$ and Hall currents may be deflecting the ion flow. $\boldsymbol{E}$ fluctuations (Figure 1j) are particularly intense. The plasma density (N_e, Figure 1k) changes in consort with the flow vortex in $\boldsymbol{V}_{Ion}$ (Figure 1h). T_i and T_e increase (Figure 1l). These features are characteristic of a turbulent BBF braking region (Ergun et al., 2015).

Shortly after the fluctuations in ***B***, $\boldsymbol{V}_{Ion}$, $\boldsymbol{V}_{Elc}$, and ***E*** subside (~21:21 UT), the MMS satellites enter the outer radiation belt. Starting at ~21:22 UT, the intensity of energetic ion and electron fluxes gradually increases whereas the fluctuations decrease. T_i and T_e also decrease. These observations insinuate that the BBF penetrated to near the outer edge of the radiation belt.

One of the most important questions about this event is if and how the intense, turbulent ***E*** locally energizes electrons and ions. As such, the nature of the turbulence and the properties of ***E*** deserve further investigation. Figure 1m displays the frequency-domain power spectral density (PSD) of ***B*** and ***E*** during the event. The circles represent the measured PSDs. The light blue lines refer to the inertial region ($f <$ ~0.4 Hz) with previously measured spectral indices (α) of turbulent BBFs. The red and green lines are fits. These ***B*** and ***E*** PSDs are remarkably similar to others in identified turbulent events in the Earth's magnetotail (Ergun et al., 2015; 2018; 2020a,b). The spectral index of ***B*** in the inertial region ($f <$ ~0.4 Hz) is consistent with -5/3; the short period makes a fit uncertain. The ion skin depth (d_i) is greater than the ion gyroradius (ρ_i) due to ~110 nT background ***B*** (mean plasma parameters are in Figure 1n). We presume that the spectral break (~0.4 Hz) is near a region where the wavevector (***k***) is such that $|\boldsymbol{k}|d_i \sim 1$. The ***E*** PSD < ~0.4 Hz is consistent with a shallow index previously observed ($\alpha = -1.25$). The electrostatic or Hall region (Franci et al., 2015) of the ***E*** PSD is between ~0.4 Hz and ~40 Hz with $\alpha \sim -0.77$ (red line in Figure 1m). At higher frequencies, the ***E*** PSD steeply declines.

From the measured PSD (P_E), one can estimate the ion heating rate to be (*Chang et al.*, 1986):

$$\dot{W}_i = \frac{e^2}{2m_i}\eta_L P_E(f_{ci}) \#1$$

Here, e is the fundamental charge, m_i is the ion mass, and η_L (~ ½) is the fraction of P_E that is left-hand polarized. Since $P_E(f_{ci}) \sim 10$ mV^2 m^{-2} Hz^{-1} (Figure 1m), $\dot{W}_i$ is estimated to be 250 eV s^{-1}, which is sufficient to explain the observed values of T_i. Investigation of energetic ions requires a much more involved analysis and is reserved for a later study.

To the contrary, there is little power at $f \geq f_{ce}$ (Figure 1m) and $E_{||}$ is small (written on plot) which, at first glance, suggests that electron energization should be negligible. Perpendicular energization requires circumvention of the first adiabatic invariant ($\mu = p_{\perp}^2/2\gamma m_o B$). However, energization can occur if the correlation length scale (d_{corr}) in the $\boldsymbol{E}$ turbulence is sufficiently small. If an electron's parallel velocity is such that $d_{corr||}/v_{||} < 1/f_{ce}$, it experiences changes in $\boldsymbol{E}$ in less than $1/f_{ce}$ in its frame and therefore can be energized perpendicular to $\boldsymbol{B}$ (Ergun et al., 2020a,b). Furthermore, if an electron's gyroradius is such that $\rho_e \geq d_{corr\perp}$, it can experience enhanced parallel energization, perpendicular energization, and pitch-angle scattering.

Figures 1o, 1p, and 1q investigate the correlation length of $\boldsymbol{E}$ beginning with the frequency range below f_{ci}, which is of interest for studying ion energization. The MMS spacecraft are separated from ~39 to ~123 km (Figure 1o). Figure 1p displays the correlation of $\boldsymbol{E}$ filtered to DC to ~1.6 Hz between each spacecraft pair. Each of the $\boldsymbol{E}$ components is separately correlated then averaged. The measured correlations support an exponential with a correlation distance of ~140 $\pm$ 50 km, which lies between ρ_i (thermal average) and d_i, as expected in a turbulent plasma.

The correlation is repeated for the frequency range of ~1.6 to ~100 Hz (Figure 1q) where energization of electrons is expected to be governed. These correlations are performed over ten, one-minute intervals for each component of $\boldsymbol{E}$ resulting in 30 individual correlations then averaged. Correlations using time lags, different periods, and/or separation of $\boldsymbol{E}_{\perp}$ and $E_{||}$ unanimously indicate that $\boldsymbol{E}$ is uncorrelated (< 0.05) at the minimum separation of 39 km, which is primarily perpendicular to $\boldsymbol{B}$. This result implies that $d_{corr} \leq$ 10 km (Figure 1q), which is consistent with d_e ~ 6 km and thermal ρ_e ~ 820 m. Since $\langle E_{\perp}\rangle_{RMS} \cong 7\ \langle E_{||}\rangle_{RMS}$, the constraint on

d_{corr} is likely that of $d_{corr\perp}$. Furthermore, even though $\partial \boldsymbol{B}/\partial t$ is visible (Figure 1c), $|\nabla \times \boldsymbol{E}| \ll \langle \boldsymbol{E} \rangle_{RMS}/d_{corr}$, so $\boldsymbol{E}$ is primarily electrostatic in this higher-frequency range (Figure 1m). Using $\nabla \times \boldsymbol{E} \approx 0$, $\langle E_{||} \rangle_{RMS}/d_{corr\perp} \approx \langle E_{\perp} \rangle_{RMS}/d_{corr||}$, which implies $d_{corr||}$ is ~7 $d_{corr\perp}$.

3. Electron Energization and Test-Particle Simulations

In a magnetized plasma, parallel and perpendicular energization are distinct and quite complex. Energizing by $E_{||}$ can be amplified if $\rho_e \geq d_{corr\perp}$, which causes an electron's orbit to transit regions of uncorrelated $E_{||}$. Perpendicular energization is often hindered since μ is conserved. However, as discussed above, if $\rho_e \geq d_{corr\perp}$ or $d_{corr||}/v_{||} < 1/f_{ce}$, an electron can experience impulses on time scales less than $1/f_{ce}$. Since $\rho_e = v_{\perp}/\omega_{ce}$, these conditions are:

$$v_{||} \geq d_{corr||} f_{ce} \text{ or } v_{\perp} \geq d_{corr\perp} \omega_{ce} \#2$$

In a turbulent environment, it is not unusual that $d_{corr\perp} \approx d_e = c/\omega_{pe}$ (ω_{pe} is the electron plasma frequency) so the condition for "full energization" (breaking of μ) can be estimated as:

$$\frac{p_{\perp}}{m_o c} \geq \frac{\omega_{ce0}}{\omega_{pe}} \text{ or } \frac{p_{||}}{m_o c} \geq \frac{\omega_{ce0}}{\omega_{pe}} R_{corr} \text{ where } R_{corr} = \left(\frac{d_{corr||}}{2\pi \, d_{corr\perp}} \right) \#3$$

Here, m_0 is the electron rest mass and ω_{ce0} represents the rest-mass electron cyclotron frequency. R_{corr}, a weighted parallel to perpendicular correlation ratio, is approximately unity in the observed event. Importantly, the conditions in Equation (3) favor higher-energy particles and therefore support acceleration. At the location of the MMS satellites, $\omega_{ce0}/\omega_{pe} \sim 0.38$, so only electrons with energies >40 keV are expected to experience full energization.

In a global-scale picture, electrons are free to travel along Earth's magnetic field lines and visit a range of values of |***B***|, so ω_{ce0}/ω_{pe} also has an appreciable range since N_e remains relatively constant far from Earth. MMS's location (Figures 2a) is off the equatorial plane, so mapping is required to determine the magnetic field line geometry. Unfortunately, the BBF presents a large disturbance making accurate mapping difficult. The measured ***B*** direction and a model are combined for a rough mapping (see supplemental material) to estimate a L-shell of ~10 $\pm$1 R_E, which, at L = 10 R_E, implies that lowest |***B***| is ~31 nT near the equator with ω_{ce0}/ω_{pe} ~ 0.11. There, only electrons with energies > ~5 keV (if isotropic) meet the conditions for full energization (Equation 3). As a result, nowhere along the field line do core electrons (< 2.5 keV) experience full energization.

To investigate electron energization by ***E*** further, we perform a quasi-1D test-particle simulation of electrons along a L = 10 R_E stretched field line (Figures 2a and 2b). The simulation code is modified from a previously-described version (Ergun et al., 2020b). The simulation domain (Z) is 3D (25 R_E x 36 d_e x 36 d_e), which is a long, narrow box. Electron velocities are tracked in 3D. The perpendicular dimensions are periodic; electrons can travel along ***B***, orbit ***B***, magnetically mirror, and receive impulses from ***E***, but cannot carry out curvature or $\nabla_\perp B$ drifts (discussed later). E_{DC} = 0 so there is no net drift.

The test-particle simulation is not self-consistent as it imposes ***E*** and constant ***B***. A key feature of the simulation, however, is that ***E*** is constructed to match the observed $\langle \boldsymbol{E} \rangle_{RMS}$, PDF (Figure 2c), spectrum (Figure 2d), and correlation lengths (Figure 1q). Since a realistic reproduction of ***E*** is central to understanding local acceleration, we provide further detail (also see Figure 6 in Ergun et al., 2020b). Reconstructed ***E*** is limited to the frequency range of ~1.6 to ~100 Hz, where most of the power lies. Since ***E*** is primarily electrostatic, a scalar potential (Φ) is pseudo-randomly assigned so that the PDF of the reconstructed $\boldsymbol{E}$ matches the observed PDF and $\langle \boldsymbol{E} \rangle_{RMS}$ (Figure 2c). Φ is on a grid with perpendicular spacing proportional to $d_{corr\perp}$. Since d_{corr} is only constrained by observations, $d_{corr\perp}$ is treated as a variable; the simulation is performed with $d_{corr\perp}$ ranging from 2 km to 10 km. As discussed earlier, the electrostatic condition enforces $d_{corr||} = d_{corr\perp} \langle E_{\perp} \rangle_{RMS} / \langle E_{||} \rangle_{RMS}$. An example of the resulting PSD versus $|\boldsymbol{k}| d_e$ ($d_{corr\perp}$= 10 km) is plotted in Figure 2d. Mapping between $|\boldsymbol{k}|$ and f with a fixed velocity of 2500 km s^{-1} (nearly V_A the Alfvén velocity, Figure 1n) yields a good match to the measured $\boldsymbol{E}$ PSD versus f (Figure 1m). As time advances, Φ is regenerated every 10 ms to 500 ms, pseudo-randomly. This imposed time variation is consistent with observations and slow compared to $1/f_{ce}$. At the equator, for example, an electron undergoes 8 to 400 orbits before Φ is altered. $\langle \boldsymbol{E} \rangle_{RMS}$ is constant between $Z = \pm 7$ R_E (Figure 2b) but is reduced at larger values of Z. MMS is located at -5.9 R_E in the simulation domain (Figure 2b). A primary assumption is that $\boldsymbol{E}$ turbulence extends through the equator, which is consistent with previous reports (e.g. Ergun et al., 2015).

The simulation is initiated with a T_e = 600 eV Maxwellian distribution (see Figure 1l at 21:10 UT) with a constant density. Electrons then evolve in time under gyration, the magnetic mirror force, and $\boldsymbol{E}$. The $\pm Z$ boundaries of the simulation are open. A particle that exits the domain is replaced by a randomly-generated thermal particle (T_e = 600 eV) at the boundary. More than 95% of particles initialized between $Z = \pm 6$ R_E remain in the simulation domain after 10 s due to the robust magnetic mirror. The simulation is tested for 50 s with $\boldsymbol{E}$ = 0 to assure conservation of energy. Tests also verify that energization is proportional $\langle E^2 \rangle$.

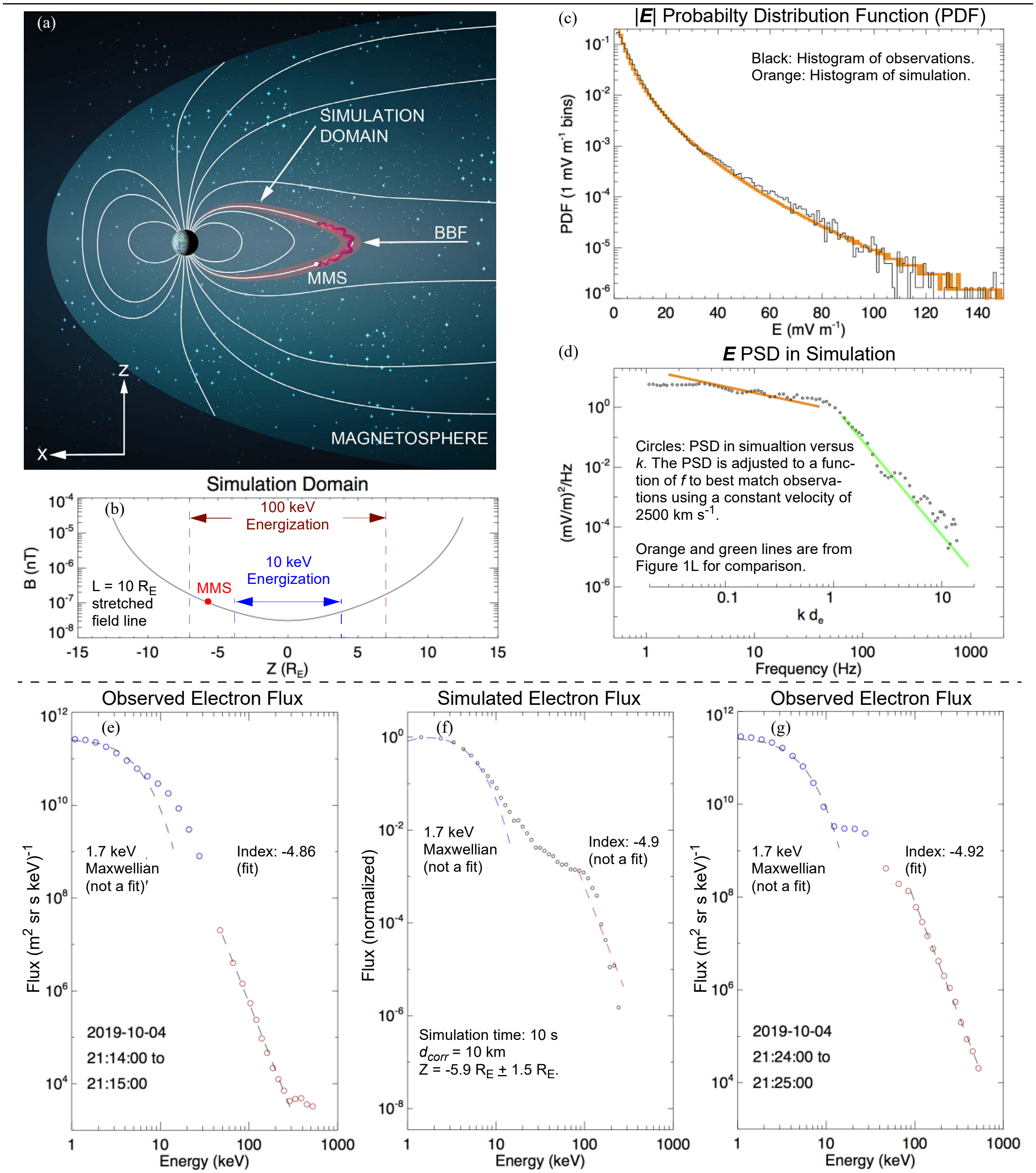

Figure 2. Details of and results from the test-particle simulation. (a) A cartoon depicting the simulation domain. (b) |***B***| in the simulation domain. (c) The PDF of |***E***| as observed (black) and in the simulation domain (orange). The near-exact match is by design. (d) An example of a PSD

versus $\boldsymbol{k}$ in the simulation (circles) and the fits to the observed PSD versus f in Figure 1m (orange and green lines). Mapping between $\boldsymbol{k}$ and f using a velocity of 2500 km s^{-1} creates the best match. (e) The electron flux as observed during the turbulent event. (f) The electron flux from the test-particle simulation with d_{corr} = 10 km at 10 s. (g) The electron flux as observed in the outer radiation belt.

After initiation, the simulation is advanced until electrons attain an energy density similar to that observed. In the simulation, curvature and $\nabla_{\perp}B$ drifts do not influence an electron's evolution. These drift speeds are proportional to energy (W) and inversely proportional to $|\boldsymbol{B}|$. A concern is that high-energy electrons drift relative to the thermal electrons and may have a different dwell times in the turbulent region. For example, a 100 keV electron trapped near the equator can drift relative to core electrons up to ~200 km s^{-1}. If the scale size of a BBF is 1 R_E, higher-energy (~100 keV) electrons separate from the core in roughly 30 s. This interval is less than the observed duration of the turbulence (~600 s; Figure 1) but greater than the simulation run times (10 s). As a result, curvature drifts and $\nabla_{\perp}B$ drifts are inconsequential in the simulation, but should be significant for data interpretation.

Figures 2e-2g compare observed electron flux (intensity) with electron flux in the simulation. On the left (Figure 2e, circles) is the observed electron flux as a function of energy complied inside of the turbulent region. The time is written in the plot. In the center (Figure 2f) is a flux distribution (Z = -5.9 $\pm$ 1 R_E) from the simulation at t = 10 s with $d_{corr\perp}$ = 10 km. On the right (Figure 2g) is an observed flux distribution from the outer radiation belt. The shapes of the simulated and observed fluxes have several common characteristics. The core of the flux distributions have a similar T_e ~1.7 keV (see dashed blue lines). Most noticeably, the observed and simulation fluxes have a "shoulder" between ~10 keV and ~100 keV and a steep power-law tail at energies >100 keV. Setting d_{corr} to < 10 km results in faster energization. Simulations suggest that $\boldsymbol{E}$, as measured and if extended along $\boldsymbol{B}$, can be responsible for local acceleration.

The simulation's ~10 s run time to reach observed electron energy levels seems fast when compared to the duration of the BBF event (600 s), but is somewhat consistent with the time that curvature and $\nabla_{\perp}B$ drifts separate electron populations. Furthermore, $\boldsymbol{V}_{ion}$ (Figure 1h), $\boldsymbol{V}_{Elc}$ (Figure 1i), and $\boldsymbol{E}$ (Figure 1j) indicate substantial Hall fields (ions are decoupled). $\boldsymbol{V}_{Elc}$ reaches 1000 km s^{-1} and often differs from $\boldsymbol{V}_{ion}$ by more than 100 km s^{-1}, which may limit an energetic electron's dwell time in the region of turbulence to ~10 s, which the simulation suggests.

There is one notable discrepancy between the simulation results and observations. The observed electron distributions are nearly isotropic (Figure 1l) whereas the simulated electron distributions have $T_{e\perp} > T_{e\|}$. This discrepancy likely results in part from the imposition of $\langle E_{\perp}\rangle_{RMS}/\langle E_{||}\rangle_{RMS} = 7$ over the entire simulation domain. This ratio is closer to 3 in turbulent BBF events nearer to the equator (Ergun et al., 2015). Additionally, coherent waves such as Alfvén and whistler waves may act to pitch angle scatter electrons (e. g. Chaston et al, 2018).

4. Discussion and Conclusions

The MMS satellites detected a turbulent BBF braking region close to the outer radiation belt. Of primary interest, T_i and T_e increase and high-energy ion and electron fluxes vary concurrently with $\boldsymbol{E}$, $\boldsymbol{B}$, and $\boldsymbol{V}_{Ion}$ suggesting local energization and acceleration.

The properties of $\boldsymbol{E}$ are investigated in detail including the spectra, correlation distance, PDF, and RMS amplitude. The four-spacecraft MMS mission constrained d_{corr} to be $\leq$ 10 km in the ~1.6 to ~100 Hz frequency range (Figure 1q). The fact that $\boldsymbol{E}$ is uncorrelated at a relatively small separation is critical. Perpendicular energization requires violation of μ conservation and there is little power in $\boldsymbol{E}$ with $f > f_{ce}$. We hypothesize that if $p_{\perp}/m_0c$ or $p_{\parallel}/m_0c$ exceed ω_{ce0}/ω_{pe}, an electron experiences changes in $\boldsymbol{E}$ faster than $1/f_{ce}$, which breaks conservation of μ. This postulation also implies that the highest-energy electrons receive more energy than do the lower-energy electrons, which leads to the development a non-thermal shoulder and energetic tail in the electron distribution.

Figure 3 illustrates the underlying process of particle acceleration by turbulent, uncorrelated, electrostatic $\boldsymbol{E}$. In the plane of the gyration, a low-energy electron (2 keV in the drawing) experiences a nearly constant $\boldsymbol{E}$ whereas a higher-energy electron (20 keV in the drawing) transits regions of changing $\boldsymbol{E}$ during its gyration. Even though $\boldsymbol{E}$ is primarily electrostatic, the particle does not necessarily return to the same location in the perpendicular plane (Figure 3a) or in the same location along $\boldsymbol{B}$ (Figure 3b) and therefore can experience energy change. The time dependence of $\boldsymbol{E}$, albeit slow, is crucial in that an electron's energy gain or loss is not limited to the largest variation in Φ. A finite $\nabla \times \boldsymbol{E}$ can enhance acceleration.

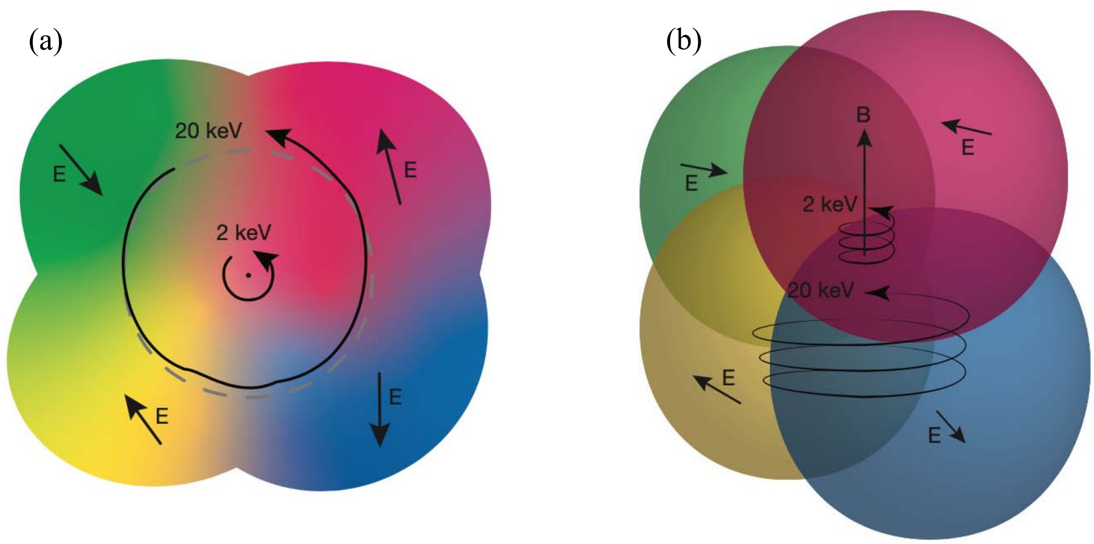

Figure 3. A drawing of electron orbits in an uncorrelated, electrostatic ***E*** illustrating how turbulent acceleration favors higher-energy electrons. (a) A view of the orbital plane. The higher-energy (20 keV) electron's orbit transits several uncorrelated regions of ***E*** (including $E_{\|}$) as it gyrates and therefore does not necessarily follow a closed path. It can gain or lose energy. A lower-energy electron (2 keV) sees very little change in ***E*** over an orbit. (b) A 3D view of an electron's helical path along ***B***. A high-energy electron can experience changes in ***E*** faster than its gyration period.

This hypothesis is tested with a quasi-1D test-particle simulation. Electrons are magnetized and therefore well represented by a 1D simulation whereas ions require a much more complex investigation. A key aspect of the simulation is the careful reproduction of the observed ***E*** including the d_{corr}, spectrum, parallel and perpendicular RMS power, and PDF. The salient result (Figures 2e-2g) is that the electron distributions develop an extended shoulder above ~10 keV and an energetic tail. Despite its short-comings, (not self-consistent, RMS ***E*** extends $\pm$7 R_E from the equator, simulation distributions are not isotropic, drifts are not included), the simulation demonstrates the feasibility of local electron acceleration.

Analytically, one can estimate electron energization rates from random impulses via Equation 7 in Ergun et al, (2020b):

$$\dot{W} \approx \frac{e^2\langle E_{Eff}^2\rangle\langle\delta t\rangle}{2\,W/c^2} \#4$$

where $W = \gamma m_0 c^2$ and $\langle E_{Eff}^2\rangle$ represents the effective RMS $\boldsymbol{E}$ (that with $f > f_{ce}$ in the electron frame) experienced along an electron's helical path. Significantly, $\langle E_{Eff}^2\rangle$ strongly increases with increasing W (Equation 3). The period of the impulses, $\langle\delta t\rangle$, is a fraction of the gyroperiod. For example, in Figure 3a, $\langle\delta t\rangle \approx 1/(4\,f_{ce})$ for the 20 keV electron. From observations, $\langle E_{Eff}^2\rangle \approx 70$ mV^2 m^{-2} and $\langle\delta t\rangle \approx 8 \times 10^{-5}$ s. A > ~20 keV electron experiences ~500 eV/s of energization on average, supporting the simulation results. Core electrons (< 2.5 keV) experience a much smaller $\langle E_{Eff}^2\rangle$ and receive significantly less energization. This analytical exercise illustrates why the electron distribution (Figure 2f) develops an extended shoulder above ~5 keV; high energy electrons receive full acceleration while core electrons are heated at a slower pace. For high-γ electrons, we note that $\langle\delta t\rangle$ is proportional to γ, so $\dot{W}$ increases with energy.

Another interesting aspect unique to electrons trapped in a dipole field is illustrated in Figure 2b. The extent along $\boldsymbol{B}$ in which an electron experiences full energization increases with an electron's energy (Equation 3). For example, a 100 keV electron is subject to full energization between $Z = \pm 7$ R_E whereas a 10 keV electron only has full energization between $Z = \pm 4$ R_E. Consequently, higher-energy electrons again receive more energy further favoring acceleration.

In conclusion, MMS observations of electron and ion acceleration from a turbulent BBF suggest local acceleration by ***E***. Electron acceleration is supported by test-particle simulation that used a realistic reproduction of the observed ***E***. The resulting enhanced shoulder and energetic tail in the electron distribution just outside of the radiation belts could supply electrons to the outer radiation belt. If these electrons are adiabatically transported closer to Earth (higher |***B***|, Gabrielse et al, 2012; Turner et al., 2015; 2016; Ukhorskiy et al., 2017; Sorathia et al., 2018; Turner et al., 2021), they can account for MeV electrons. A more far-reaching conclusion is that, since turbulence is pervasive in plasmas, it is likely a significant contributor to charged particle acceleration.

Acknowledgements

Article is supported by NASA's MMS (NNG04EB99C) and THEMIS (NAS5-02099) missions. DLT received support from NASA grant 80NSSC19K0280, and DLT and MEU thank the International Space Sciences Institute for support. JES is supported by the Royal Society University Research Fellowship URF\R1\201286.

Data Availability Statement

The MMS data set is available at https://lasp.colorado.edu/mms/sdc/public/datasets/.

References

Angelopoulos, V., W. Baumjohann, C. F. Kennel, F. V. Coroniti, M. G. Kivelson, R. Pellat, R. J. Walker, H. Lühr, and G. Paschmann (1992), Bursty bulk flows in the inner central plasma sheet, *J. Geophys. Res*., 97(A4), 4027–4039, doi:10.1029/91JA02701

Angelopoulos, V., Kennel, C. F., Coroniti, F. V., Pellat, R., Kivelson, M. G., Walker, R. J., … Gosling, J. T. (1994). Statistical characteristics of bursty bulk flow events. *Journal of Geophysical Research*, 99(A11), 21,257– 21,280. https://doi.org/10.1029/94JA01263

Baumjohann, W., G. Paschmann, and C. A. Cattell (1989), Average plasma properties in the central plasma sheet, *J. Geophys. Res*., 94(A6), 6597–6606, doi:10.1029/JA094iA06p06597

Birn, J., M. F. Thomsen, J. E. Borovsky, G. D. Reeves, D. J. McComas, and R. Belian (1997), Characteristic plasma properties during dispersionless substorm injections at geosynchronous orbit, J. Geophys. Res., 102(A2), 2309– 2324, doi:10.1029/96JA02870.

Burch, J. L., Moore, T. E., Torbert, R. B., & Giles, B. L. (2016). Magnetospheric Multiscale overview and science objectives. Space Science Reviews. https://doi.org/10.1007/s11214-015-0164-9

Chang, T., Crew, G. B., Hershkowitz, N., Jasperse, J. R., Retterer, J. M., & Winningham, J. D. (1986). Transverse acceleration of oxygen ions by electromagnetic ion cyclotron resonance with broad band left-hand polarized waves. *Geophysical Research Letters*, 13(7), 636– 639. https://doi.org/10.1029/GL013i007p00636

Chaston, C. C., Bonnell, J. W., Halford, A. J., Reeves, G. D., Baker, D. N., Kletzing, C. A., & Wygant, J. R. (2018). Pitch angle scattering and loss of radiation belt electrons in broadband electromagnetic waves. *Geophysical Research Letters*, 45, 9344– 9352. https://doi.org/10.1029/2018GL079527

Dubyagin, S., V. Sergeev, S. Apatenkov, V. Angelopoulos, A. Runov, R. Nakamura, W. Baumjohann, J. McFadden, and D. Larson (2011), Can flow bursts penetrate into the inner magnetosphere?, *Geophys. Res. Lett*., 38, L08102, doi:10.1029/2011GL047016.

Ergun, R. E., K. A. Goodrich, J. E. Stawarz, L. Andersson, and V. Angelopoulos (2015), Large-amplitude electric fields associated with bursty bulk flow braking in the Earth's plasma sheet. *J. Geophys. Res. Space Physics*, 120, 1832–1844. doi: 10.1002/2014JA020165

Ergun, R. E., Tucker, S., Westfall, J., Goodrich, K. A., Malaspina, D. M., Summers, D., … Cully, C. M. (2016). The axial double probe and fields signal processing for the MMS mission. *Space Science Reviews*. https://doi.org/10.1007/s11214-014-0115-x

Ergun, R. E., Goodrich, K. A., Wilder, F. D., Ahmadi, N., Holmes, J. C., Eriksson, S., Stawarz, J. E., Nakamura, R., Genestreti, K. J., Hesse, M., & Burch, J. L. (2018). Magnetic reconnection, turbulence, and particle acceleration: Observations in the Earth's magnetotail. *Geophysical Research Letters*, 45, 3338– 3347. https://doi.org/10.1002/2018GL076993

Ergun, R. E., Ahmadi, N., Kromyda, L., Schwartz, S. J., Chasapis, A., Hoilijoki, S., Wilder, F. D., Stawarz, J. E., Goodrich, K. A., Turner, D. L., Cohen, I. J., Bingham, S. T., Holmes, J. C., Nakamura, R., Pucci, F., Torbert, R. B., Burch, J. L., Lindqvist, P. A., Strangeway, R. J., le Contel, O., & Giles, B. L. (2020a). Observations of particle acceleration in magnetic reconnection-driven turbulence. *The Astrophysical Journal*, 898(2), 154. https://doi.org/10.3847/1538-4357/ab9ab6

Ergun, R. E., Ahmadi, N., Kromyda, L., Schwartz, S. J., Chasapis, A., Hoilijoki, S., et al. (2020b). Particle acceleration in strong turbulence in the Earth's magnetotail. *The Astrophysical Journal*, 898(15), 153. https://doi.org/10.3847/1538-4357/ab9ab5

Franci, L., Landi, S., Matteini, L., Verdini, A., & Hellinger, P. (2015). High-resolution hybrid simulations of kinetic plasma turbulence at proton scales. *The Astrophysical Journal*, 812, 21. https://doi.org/10.1088/0004-637X/812/1/21

Gabrielse, C., Angelopoulos, V., Runov, A., & Turner, D. L. (2012). The effects of transient, localized electric fields on equatorial electron acceleration and transport toward the inner magnetosphere. *Journal of Geophysical Research*, 117, A10213. https://doi.org/10.1029/2012JA017873

LeContel, O., Leroy, P., Roux, A., Coillot, C., Alison, D., Bouabdellah, A., … de la Porte, B. (2016). The Search-Coil Magnetometer for MMS. *Space Science Reviews*, 199, 257– 282. https://doi.org/10.1007/s11214-014-0096-9

Lindqvist, P.-A. *et al*. (2016), The spin-plane double probe instrument for MMS, *Space Sci. Rev.* 199, 137-165, doi:10.1007/s11214-014-0116-9.

Liu, J., Angelopoulos, V., Zhang, X.-J., Turner, D. L., Gabrielse, C., Runov, A., et al. (2016). Dipolarizing flux bundles in the cis-geosynchronous magnetosphere: Relationship between electric fields and energetic particle injections. Journal of Geophysical Research: Space Physics, 121(2), 1362– 1376. https://doi.org/10.1002/2015JA021691

Nakamura, R., W. Baumjohann, R. Schvdel, M. Brittnacher, V. A. Sergeev, M. Kubyshkina, T. Mukai, and K. Liou (2001), Earthward flow bursts, auroral streamers, and small expansions, *J. Geophys. Res*., 106, 10,791– 10,802, doi:10.1029/2000JA000306

Nakamura, R., et al. (2009), Evolution of dipolarization in the near-Earth current sheet induced by Earthward rapid flux transport, *Ann. Geophys*., 27, 1743– 1754

Mauk, B. H., et al. (2016), The energetic Particle Detector (EPD) investigation and the Energetic Ion Spectrometer (EIS) for the Magnetospheric Multiscale (MMS) mission, *Space Sci. Rev.*, 199(1), 471–514, doi:10.1007/s11214-014-0055-5

Ohtani, S., H. J. Singer, and T. Mukai (2006), Effects of the fast plasma sheet flow on the geosynchronous magnetic configuration: Geotail and GOES coordinated study, *J. Geophys. Res.*, 111, A01204, doi:10.1029/2005JA011383

Pollock, C., Moore, T., Jacques, A., Burch, J., Gliese, U., Saito, Y., … Zeuch, M. (2016). Fast Plasma Investigation for Magnetospheric Multiscale. *Space Science Reviews*, 199, 331– 406. https://doi.org/10.1007/s11214-016-0245-4

Runov, A., V. Angelopoulos, M. I. Sitnov, V. A. Sergeev, J. Bonnell, J. P. McFadden, D. Larson, K.-H. Glassmeier, and U. Auster (2009), THEMIS observations of an earthward-propagating dipolarization front, *Geophys. Res. Lett.*, 36, L14106, doi:10.1029/2009GL038980

Runov, A., V. Angelopoulos, X.-Z. Zhou, X.-J. Zhang, S. Li, F. Plaschke, and J. Bonnell (2011), A THEMIS multicase study of dipolarization fronts in the magnetotail plasma sheet, *J. Geophys. Res.*, 116, A05216, doi:10.1029/2010JA016316

Russell, C. T., Anderson, B. J., Baumjohann, W., Bromund, K. R., Dearborn, D., Fischer, D., … Richter, I. (2016). The Magnetospheric Multiscale magnetometers. *Space Science Reviews*, 199, 189– 256. https://doi.org/10.1007/s11214-014-0057-3

Sergeev, V. A., K. Liou, C.-I. Meng, P. T. Newell, M. Brittnacher, G. Parks, and G. D. Reeves (1999), Development of auroral streamers in association with localized impulsive injections to the inner magnetotail, *Geophys. Res. Lett.*, 26(3), 417– 420, doi:10.1029/1998GL900311

Sergeev, V. A., et al. (2000), Multiple-spacecraft observation of a narrow transient plasma jet in the Earth's plasma sheet, *Geophys. Res. Lett.*, 27(6), 851– 854, doi:10.1029/1999GL010729

Sergeev, V. A., Chernyaev, I. A., Dubyagin, S. V., Miyashita, Y., Angelopoulos, V., Boakes, P. D., Nakamura, R., and Henderson, M. G. (2012), Energetic particle injections to geostationary orbit: Relationship to flow bursts and magnetospheric state, *J. Geophys. Res.*, 117, A10207, doi:10.1029/2012JA017773.

Sergeev, V. A., Chernyaev, I. A., Angelopoulos, V., Runov, A. V., & Nakamura, R. (2014). Stopping flow bursts and their role in the generation of the substorm current wedge. *Geophysical Research Letters*, 41, 1106– 1112. https://doi.org/10.1002/2014GL059309

Sitnov, M. I., Swisdak, M., & Divin, A. V. (2009). Dipolarization fronts as a signature of transient reconnection in the magnetotail. *Journal of Geophysical Research*, 114, A04202. https://doi.org/10.1029/2008JA013980

Sorathia, K. A., Ukhorskiy, A. Y., Merkin, V. G., Fennell, J. F., & Claudepierre, S. G. (2018). Modeling the depletion and recovery of the outer radiation belt during a geomagnetic storm: Combined MHD and test particle simulations. Journal of Geophysical Research: Space Physics, 123(7), 5590– 5609. https://doi.org/10.1029/2018JA025506

Stawarz, J. E., Ergun, R. E., & Goodrich, K. A. (2015). Generation of high-frequency electric field activity by turbulence in the Earth's magnetotail. *Journal of Geophysical Research: Space Physics*, 120, 1845– 1866. https://doi.org/10.1002/2014JA020166

Takada, T., R. Nakamura, W. Baumjohann, Y. Asano, M. Volwerk, T. L. Zhang, B. Klecker, H. Réme, E. A. Lucek, and C. Carr (2006), Do BBFs contribute to inner magnetosphere dipolarizations: Concurrent Cluster and Double Star observations, *Geophys. Res. Lett*., 33, L21109, doi:10.1029/2006GL027440

Torbert, R. B., Russell, C. T., Magnes, W., Ergun, R. E., Lindqvist, P.-A., LeContel, O., … Lappalainen, K. (2016). The FIELDS instrument suite on MMS: Scientific objectives, measurements, and data products. *Space Science Reviews*, 199, 105– 135. https://doi.org/10.1007/s11214-014-0109-8

Tsyganenko, N. A., & Stern, D. P. (1996). Modeling the global magnetic field of the large-scale

Birkeland current systems. Journal of Geophysical Research, 101(A12), 27187– 27198. https://doi.org/10.1029/96JA02735

Turner, D. L., Claudepierre, S. G., Fennell, J. F., O'Brien, T. P., Blake, J. B., Lemon, C., Gkioulidou, M., Takahashi, K., Reeves, G. D., Thaller, S., Breneman, A., Wygant, J. R., Li, W., Runov, A., and Angelopoulos, V. (2015), Energetic electron injections deep into the inner magnetosphere associated with substorm activity. *Geophys. Res. Lett.*, 42, 2079– 2087. doi: 10.1002/2015GL063225

Turner, D. L., Fennell, J. F., Blake, J. B., Clemmons, J. H., Mauk, B. H., Cohen, I. J., … Burch, J. L. (2016). Energy limits of electron acceleration in the plasma sheet during substorms: A case study with the Magnetospheric Multiscale (MMS) mission. *Geophysical Research Letters*, 43, 7785– 7794. https://doi.org/10.1002/2016GL069691

Turner D. L., Cohen I. J., Michael A., Sorathia K., Merkin S., Mauk B. H., Ukhorskiy S., et al., 2021, Can Earth's Magnetotail Plasma Sheet Produce a Source of Relativistic Electrons for the Radiation Belts? *Geophysical Research Letters*, 45, e95495. doi:10.1029/2021GL095495

Ukhorskiy, A. Y., Sitnov, M. I., Merkin, V. G., Gkioulidou, M., & Mitchell, D. G. (2017). Ion acceleration at dipolarization fronts in the inner magnetosphere. *Journal of Geophysical Research: Space Physics*, 122, 3040– 3054. https://doi.org/10.1002/2016JA023304

Usanova, M. E. and Ergun R. E. (2022). Electron Energization by Turbulent Electric Fields: A Possible Source of the Outer Radiation Belt (preprint). https://essoar.org (2022), doi: 10.1002/essoar.10510040.1

Zhang, L. Q., W. Baumjohann, C. Wang, L. Dai, and B. B. Tang (2016), Bursty bulk flows at different magnetospheric activity levels: Dependence on IMF conditions, J. Geophys. Res. Space Physics, 121, 8773–8789, doi:10.1002/ 2016JA022397.

Figure Captions

Figure 1. MMS1 observations of a BBF penetrating close to the outer radiation belt. The horizonal axis on the left column is 50 minutes in time. Vectors are in GSM coordinates; colors represent components as marked on the right of a panel. (a) $\boldsymbol{B}$ at 62.5 ms resolution. The black trace is $|\boldsymbol{B}|$. (b) A magnified view of B_x. (c) $\boldsymbol{B}$ detrended by 10 s. (d) Ion flux as a function of energy (vertical axis) from 70 to 600 keV. These data are from all four MMS spacecraft. (e) Differential ion energy flux as a function of energy from 3 eV to 25 keV. (f) Electron flux from 60 to 500 keV. (g) Differential electron energy flux 6 eV to 25 keV. (h) $\boldsymbol{V}_{Ion}$ at 4.5 s resolution. (i) $\boldsymbol{V}_{Elc}$ at 4.5 s resolution smoothed over 13.5 s. (j) $\boldsymbol{E}$ at 31.25 ms resolution. (k) Electron density at 4.5 s resolution. (l) T_i and T_e at 4.5 s resolution. (m) The PSD of $\boldsymbol{B}$ and $\boldsymbol{E}$ versus frequency. (n) Average plasma conditions. (o) The relative positions of the MMS spacecraft. (p) The cross-correlation of $\boldsymbol{E}$ between the MMS spacecraft plotted as a function of separation. $\boldsymbol{E}$ is filtered from DC to 1.6 Hz. (q) The cross-correlation of $\boldsymbol{E}$ filtered from 1.6 Hz to 100 Hz.

Figure 2. Details of and results from the test-particle simulation. (a) A cartoon depicting the simulation domain. (b) $|\boldsymbol{B}|$ in the simulation domain. (c) The PDF of $|\boldsymbol{E}|$ as observed (black) and in the simulation domain (orange). The near-exact match is by design. (d) An example of a PSD versus $\boldsymbol{k}$ in the simulation (circles) and the fits to the observed PSD versus f in Figure 1m (orange and green lines). Mapping between $\boldsymbol{k}$ and f using a velocity of 2500 km s^{-1} creates the best match. (e) The electron flux as observed during the turbulent event. (f) The electron flux from the test-particle simulation with d_{corr} = 10 km at 10 s. (g) The electron flux as observed in the outer radiation belt.

Figure 3. A drawing of electron orbits in an uncorrelated, electrostatic ***E*** illustrating how turbulent acceleration favors higher-energy electrons. (a) A view of the orbital plane. The higher-energy (20 keV) electron's orbit transits several uncorrelated regions of ***E*** (including $E_{\|}$) as it gyrates and therefore does not follow a closed path. It can gain or lose energy. A lower-energy electron (2 keV) sees little change in ***E*** over an orbit. (b) A 3D view of an electron's helical path along ***B***. A high-energy electron can experience changes in ***E*** faster than its gyration period.

Figure 1.

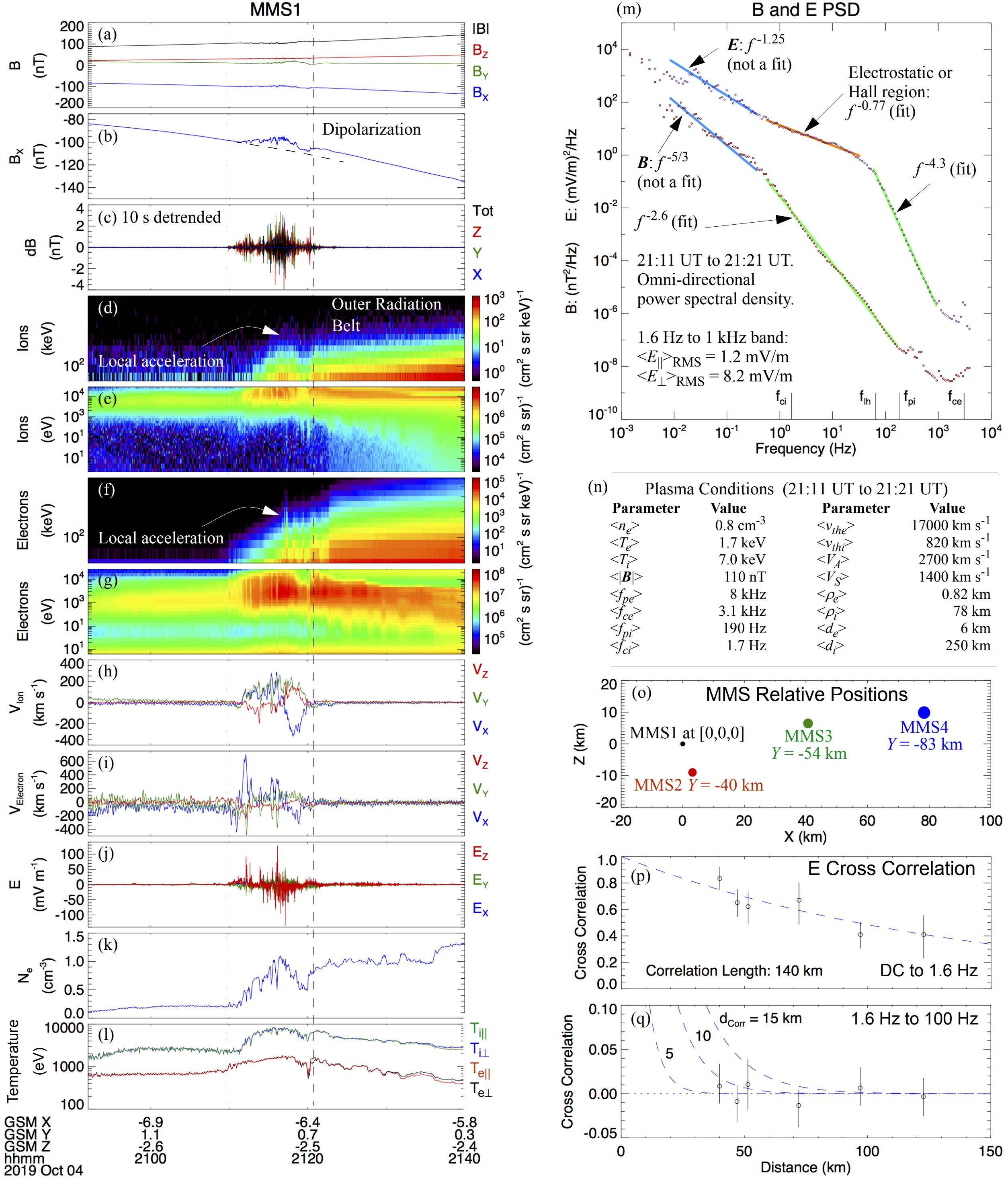

MMS1
(a)
B (nT)
|B|
BZ
BY
BX
(b)
BX (nT)
Dipolarization
(c) 10 s detrended
dB (nT)
Tot
Z
Y
X
(d)
Ions (keV)
Outer Radiation Belt
Local acceleration
(cm² s sr keV)⁻¹
(e)
Ions (eV)
(cm² s sr)⁻¹
(f)
Electrons (keV)
Local acceleration
(cm² s sr keV)⁻¹
(g)
Electrons (eV)
(cm² s sr)⁻¹
(h)
VIon (km s⁻¹)
VZ
VY
VX
(i)
VElectron (km s⁻¹)
VZ
VY
VX
(j)
E (mV m⁻¹)
EZ
EY
EX
(k)
Ne (cm⁻³)
(l)
Temperature (eV)
Ti||
Ti⊥
Te||
Te⊥
GSM X -6.9 -6.4 -5.8
GSM Y 1.1 0.7 0.3
GSM Z -2.6 -2.5 -2.4
hhmm 2100 2120 2140
2019 Oct 04
(m) B and E PSD
E: f^-1.25 (not a fit)
Electrostatic or Hall region: f^-0.77 (fit)
B: f^-5/3 (not a fit)
f^-4.3 (fit)
f^-2.6 (fit)
21:11 UT to 21:21 UT. Omni-directional power spectral density.
1.6 Hz to 1 kHz band:
<E||>RMS = 1.2 mV/m
<E⊥>RMS = 8.2 mV/m
fci
flh
fpi
fce
E: (mV/m)²/Hz
B: (nT²/Hz)
Frequency (Hz)
(n) Plasma Conditions (21:11 UT to 21:21 UT)
Parameter Value Parameter Value
<ne> 0.8 cm⁻³ <vthe> 17000 km s⁻¹
<Te> 1.7 keV <vthi> 820 km s⁻¹
<Ti> 7.0 keV <VA> 2700 km s⁻¹
<|B|> 110 nT <VS> 1400 km s⁻¹
<fpe> 8 kHz <ρe> 0.82 km
<fce> 3.1 kHz <ρi> 78 km
<fpi> 190 Hz <de> 6 km
<fci> 1.7 Hz <di> 250 km
(o) MMS Relative Positions
MMS1 at [0,0,0]
MMS3 Y = -54 km
MMS4 Y = -83 km
MMS2 Y = -40 km
Z (km)
X (km)
(p) E Cross Correlation
Cross Correlation
Correlation Length: 140 km
DC to 1.6 Hz
(q)
dCorr = 15 km
10
5
1.6 Hz to 100 Hz
Cross Correlation
Distance (km)

Figure 2.

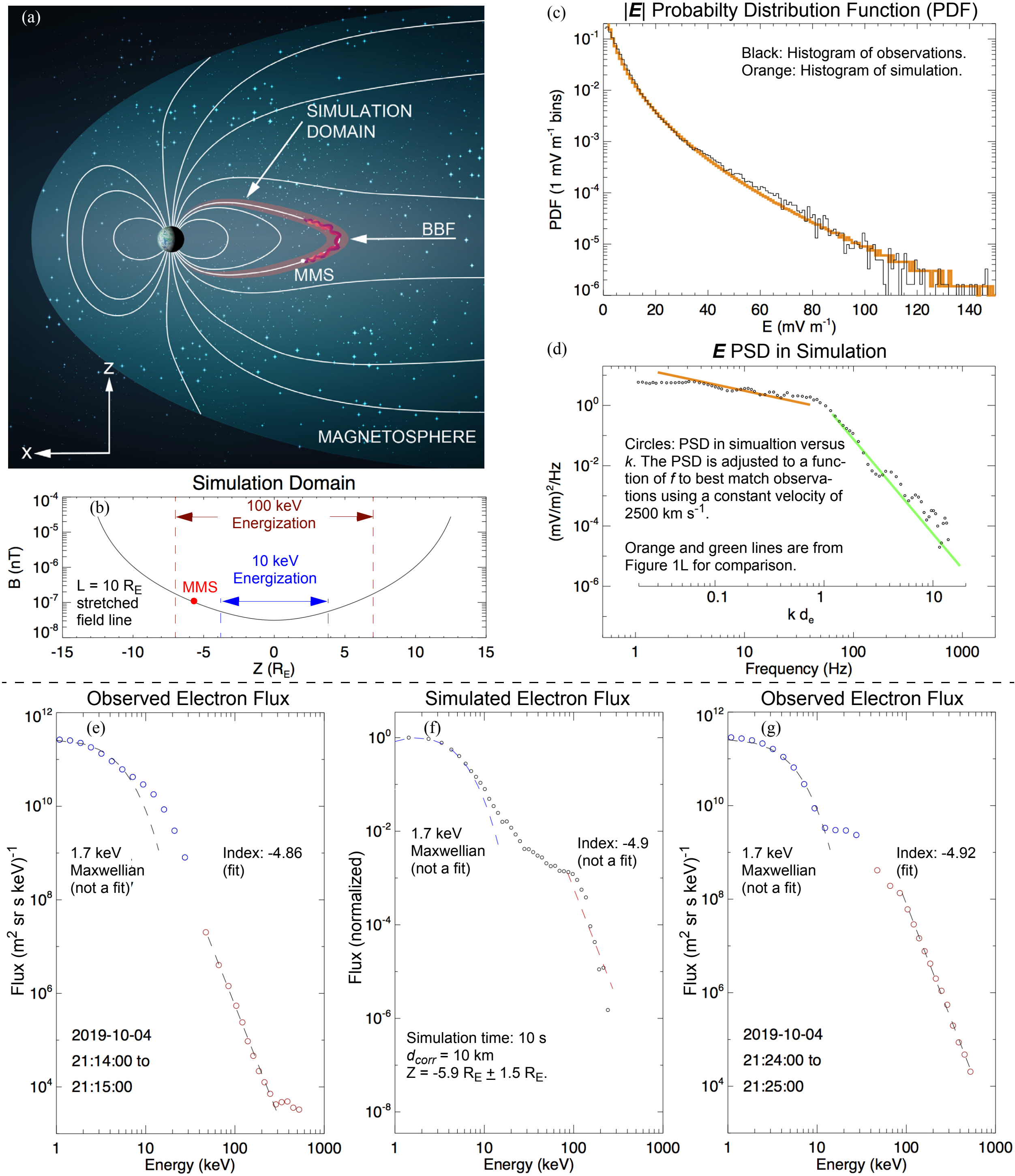

(a)
SIMULATION DOMAIN
BBF
MMS
Z
X
MAGNETOSPHERE
Simulation Domain
(b)
100 keV Energization
10 keV Energization
L = 10 R_E stretched field line
MMS
B (nT)
Z (R_E)
(c)
|E| Probabilty Distribution Function (PDF)
Black: Histogram of observations.
Orange: Histogram of simulation.
PDF (1 mV m^-1 bins)
E (mV m^-1)
(d)
E PSD in Simulation
Circles: PSD in simualtion versus k. The PSD is adjusted to a function of f to best match observations using a constant velocity of 2500 km s^-1.
Orange and green lines are from Figure 1L for comparison.
(mV/m)^2/Hz
k d_e
Frequency (Hz)
Observed Electron Flux
(e)
1.7 keV Maxwellian (not a fit)
Index: -4.86 (fit)
2019-10-04
21:14:00 to
21:15:00
Flux (m^2 sr s keV)^-1
Energy (keV)
Simulated Electron Flux
(f)
1.7 keV Maxwellian (not a fit)
Index: -4.9 (not a fit)
Simulation time: 10 s
d_corr = 10 km
Z = -5.9 R_E ± 1.5 R_E.
Flux (normalized)
Energy (keV)
Observed Electron Flux
(g)
1.7 keV Maxwellian (not a fit)
Index: -4.92 (fit)
2019-10-04
21:24:00 to
21:25:00
Flux (m^2 sr s keV)^-1
Energy (keV)

Figure 3.

(a)

(b)